Monoclinic SrIrO$_3$: an easily-synthesized conductive perovskite oxide with outstanding performance for overall water splitting in alkaline solution

Jie Yu,[†,‡] Xinhao Wu,[†] Daqin Guan,[†] Zhiwei Hu,[§] Shih-Chang Weng,[||] Hainan Sun,[†] Yufei Song,[†] Ran Ran,[†] Wei Zhou,[*,†] Meng Ni,[‡] and Zongping Shao[*,†,⊥]

[†]Jiangsu National Synergetic Innovation Center for Advanced Materials (SICAM), State Key Laboratory of Materials-Oriented Chemical Engineering, College of Chemical Engineering, Nanjing Tech University, No. 30 Puzhu South Road, Nanjing 211800, P. R. China

[‡]Building Energy Research Group, Department of Building and Real Estate, The Hong Kong Polytechnic University, Hung Hom, Kowloon, 999077, Hong Kong, China

[§]Max Planck Institute for Chemical Physics of Solids, Nothnitzer Strasse 40, Dresden 01187, Germany

[||]National Synchrotron Radiation Research Center, 101 Hsin-Ann Road, Hsinchu 30076, Taiwan

[⊥]Department of Chemical Engineering, Curtin University, Perth, Western Australia 6845, Australia

ABSTRACT: Fabricating efficient bifunctional catalysts for both hydrogen/oxygen evolution reactions (HER/OER) in an easy and mass-productive way is highly attractive for alkaline water electrolyzers. Perovskite oxides show compositional flexibility and high property tunability, while poor electrical conductivity and relatively low HER activity hamper their application in overall water splitting. Here, a conductive monoclinic SrIrO$_3$ perovskite is developed as an excellent alkaline electrocatalyst with bifunctionality that can be easily synthesized under normal conditions. Toward HER, it experiences progressive surface self-reconstruction during the activation process due to lattice Sr^{2+} leaching, eventually leading to a remarkable apparent activity with an approximately 11-fold enhancement at 200 mV overpotential relative to the fresh sample. Experimental and theoretical evidence reveals that etching of lattice Sr^{2+} in relatively less stable SrIrO$_3$ compared to IrO$_2$ is crucial for triggering this self-reconstruction. Toward OER, no obvious surface reconstruction occurs, and an overpotential of only 300 mV is required to realize 10 mA cm$^{-2}_{geo}$, significantly lower than most perovskites reported previously (340-450 mV). The activated SrIrO$_3$ from HER operation can be used alternatively as an OER electrocatalyst with further improved performance. A SrIrO$_3$-based two-electrode water-splitting cell shows exceptional performance, i.e., 1.59 V@10 mA cm$^{-2}_{geo}$ with negligible performance degradation over 10 h.

1. INTRODUCTION

Electrochemical water splitting (EWS), which allows the conversion of electricity generated from intermittent renewable energy, such as solar and wind power, into storable hydrogen fuel with high purity, has been such a fascinating one in various environmental-friendly alternative energy conversion/storage technologies. [1-3] The economic competitiveness of hydrogen production through EWS with the currently mature technologies, such as methane/coal steam reforming, is, however, highly dependent on the electrode performance. [4-7] In a typical water-splitting electrolyzer, the hydrogen evolution reaction (HER) and oxygen evolution reaction (OER) occur at the cathode and anode, respectively, but the sluggish reaction rates at both electrodes greatly reduce the coulombic efficiency, thus decreasing the competitiveness of this technology for hydrogen production. [7, 8] To accelerate both half reactions, it is of paramount importance to exploit efficient electrocatalysts. Due to the different reaction conditions, varied reaction intermediates, and multiple reaction steps, different catalysts are usually used for HER and OER. [9, 10] For example, to date, Pt-involving materials demonstrate benchmark HER activity in both alkaline and acidic electrolytes, [5] and Ru/Ir-based materials, especially IrO$_2$ and RuO$_2$, are the benchmark

electrocatalysts for OER. [11] However, to further simplify water-splitting electrolyzers and reduce the corresponding cost, an electrocatalyst with bifunctionality (here, bifunctionality refers to the ability to simultaneously facilitate the OER and HER) is highly desirable. [12, 13]

An important type of functional compound, perovskite oxides with the general formula ABO$_3$, in which the A and B sites are occupied by rare-earth/alkaline-earth metal elements and transition metal elements, respectively, are characterized by high compositional and structural tenability, rich properties, favourable stability, and the capability of precise control of doping sites and amounts. [14, 15] For instance, Zhu et al. found that the relatively low poor conductivity in perovskite oxides could be ameliorated well by ion doping, in situ exsolution of the B-site metal, or creating vacancies, et al., so as to optimize the catalytic behaviour. [15-17] It was also reported that a smaller particle size could have a remarkable impact on rationalizing the catalytic activities of bulk perovskites, owing to more exposed active sites. [18] During the past, perovskite oxides have shown a wide range of application potentials. [18] More recently, they have been demonstrated to be promising OER catalysts, mainly performing in an alkaline environment. [19, 20] Nevertheless, most perovskite oxides generally

demonstrate poor HER catalytic properties owing to their insufficient electrical conductivity and inappropriate Gibbs adsorption energy for hydrogen. [21, 22] Thus far, there are only a few studies about perovskite oxides as HER catalysts, such as $Pr_{0.5}(Ba_{0.5}Sr_{0.5})_{0.5}Co_{0.8}Fe_{0.2}O_{3-\delta}$ (Pr0.5BSCF) and $SrCo_{0.7}Fe_{0.25}Mo_{0.05}O_{3-\delta}$ (SCFM0.05). [23, 24] Regarding overall water splitting, nanostructuring perovskite oxide through electrospinning method has been applied, delivering favourable performance. [25, 26] However, the fabrication cost is inevitably increased by using nanostructured electrodes, and the poor intrinsic activity of perovskite for HER is unchanged. Poor electronic conductivity is another challenge for perovskite oxides in electrocatalysis. The development of bulk-phase perovskite oxide with high conductivity and intrinsic activity for both the OER and HER can greatly accelerate the practical application of electrochemical water splitting for hydrogen production.

During the past, most active HER electrocatalysts were metal-based, while few oxides possessed favourable HER activity. [27] Very recently, we have demonstrated that, through tuning the electronic structure via doping strategy, perovskite oxides can also be developed into favourable electrocatalysts for HER. [23, 24, 28, 29] For example, owing to a synergistic interplay between ordered oxygen vacancies and O 2p ligand holes to produce a near-ideal HER reaction path for water adsorption and hydrogen desorption, $RBaCo_2O_{5.5+\delta}$ double perovskite showed favorable activity for HER. [28] On the other hand, some catalysts including perovskite oxides experienced surface self-reconstruction during electrocatalysis, which could boost the activity. [30-35] Simultaneous structural tuning and surface reconstruction may then provide a useful strategy for developing high-performance bi-functional perovskite-type electrocatalysts for overall water splitting.

In this study, we report a conductive perovskite-based electrocatalyst for overall water splitting with prominent activity among perovskite materials for both the HER and OER in alkaline solution. The electrocatalyst is built from metallic $SrIrO_3$ perovskite in a monoclinic structure, which can be facilely synthesized under normal conditions. The perovskite can undergo surface self-reconstruction during the HER process due to the etching of lattice Sr^{2+}, which results in the gradual formation of a more active component, strengthened electrical conductivity, and increased active surface areas. The surface-reconstructed $SrIrO_3$ perovskite showed superior HER activity and robust stability in alkaline electrolytes, featuring a low overpotential of 139 mV to reach 10 mA cm^{-2}_{geo} (geo-geometric area of the electrode), a small Tafel slope of 49 mV dec^{-1} and a long-term stable testing for 180 h, comparable to that of Pt/C and also ranking among the best alkaline HER electrocatalysts. The monoclinic $SrIrO_3$ perovskite in the bulk phase also delivered a distinguished OER performance with an overpotential of only 300 mV at 10 mA cm^{-2}_{geo}, largely outperforming benchmark IrO_2 and available perovskite electrocatalysts. If the electrode was previously activated through HER-induced surface reconstruction, a further reduction in the overpotential of around 15 mV at a current density of 10 mA cm^{-2}_{geo} for the OER was observed. By applying the conductive $SrIrO_3$ perovskite as an electrocatalyst for overall water splitting,

a low potential of nearly 1.59 V was needed to yield a constant current density of 10 mA cm^{-2}_{geo}, fairly close to that of the benchmark Pt/C-IrO_2 couple, and no obvious performance degradation was observed during 10 h of operation.

2. RESULTS AND DISCUSSION

Perovskite materials may take different structures, depending on the synthesis conditions. The pseudo-cubic $SrIrO_3$ perovskite is a metallic conductor with a resistivity lower than 10^{-3} ohm cm at room temperature for a thin film, [36, 37] and was recently demonstrated to be an excellent electrocatalyst for OER in acidic conditions. However, pseudo-cubic $SrIrO_3$ is synthesized under demanding conditions, such as via high-pressure/high-temperature routes, or by lattice matching with pulsed laser deposition or molecular beam epitaxy, [37, 38] making it difficult to use in practical applications. Here, monoclinic $SrIrO_3$ perovskite in the bulk phase was prepared under normal conditions (a solid-state reaction performed at ambient pressure). [39] Shown in Figure 1a is the room-temperature X-ray diffraction (XRD) pattern, and the corresponding Rietveld refined results are given in Figure S1 and Table S1. All diffraction peaks were well indexed to the standard pattern of JCPDS-25-0897, confirming the successful formation of phase-pure monoclinic $SrIrO_3$ with the space group of C2/c. On the basis of Rietveld refinement of the XRD pattern, Figure 1b schematically describes the local atomic arrangement in monoclinic $SrIrO_3$, in which face-linked and corner-linked [IrO6] octahedrons are alternatively arranged along the *c*-direction. According to the scanning electron microscopy (SEM) images in Figure 1c and Figure S2a, the as-prepared $SrIrO_3$ perovskite took the form of irregular and large particles with several micrometres in size. This badly sintered sample is a result of the high calcination temperature, which was further supported by the low Brunauer–Emmett–Teller (BET) surface area based on nitrogen-adsorption/desorption measurements (Figure S2b). Figure 1d-f present the results of further close observation from high-resolution transmission electron microscopy (HRTEM). The clear interplanar distances of about 0.454 nm and 0.483 nm in Figure 1e coincide well with the spacings of the (021) and (110) facets of $SrIrO_3$ perovskite oxide, respectively. In addition, the selected-area electron-diffraction (SAED) pattern in Figure 1f also clearly discloses the diffraction spots with tetragonal arrangements along the [1-12] zone axes. All the HRTEM results reconfirmed the crystal phase structure of $SrIrO_3$. [40] Based on a 4-probe DC conductivity measurement, the conductivity of a 71 % densified monoclinic $SrIrO_3$ bar showed an apparent conductivity of ~ 65 S cm^{-1}, suggesting its metallic nature. This is highly attractive since most perovskite oxides show poor conductivity at room temperature.

The potential application of the as-prepared metallic bulk-phase monoclinic $SrIrO_3$ perovskite as an electrocatalyst for HER in alkaline solution was first assessed by using a glassy carbon (GC) electrode in an Ar-saturated potassium hydroxide solution (0.1 M, pH = 13.6). Following several previous studies, [23-25] an activation process based on cyclic voltammetry (CV) cycling was first

employed to bring the measured sample to a stable state, and the respective polarization curves were then recorded by using linear sweep voltammetry (LSV) to reflect the real HER activities. As it is well known, unlike Mo-based carbides/nitrides, perovskite oxides are relatively stable HER electrocatalysts in alkaline electrolytes, and thus, their activation process is usually fast and without obvious changes. [23, 28, 41, 42] Very interestingly, the as-prepared $SrIrO_3$ perovskite oxide initially exhibited a low HER activity, while a dramatic enhancement of the HER activity was achieved after CV activation, as shown in Figure 2a and b (the activated sample is denoted as AC-sample), specifically reducing the overpotential from 391 mV for fresh $SrIrO_3$ to 139 mV for AC-$SrIrO_3$ to reach a current density of 10 mA cm^{-2}_{geo} (η_{10}).
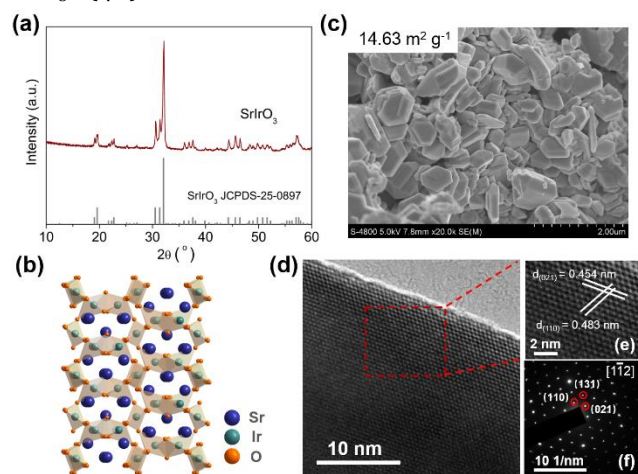

Figure 1. (a) Typical XRD pattern, and (b) schematic description of local crystal structure of the as-synthesized $SrIrO_3$ perovskite oxide. (c) corresponding SEM image, (d, e) HRTEM images, and (f) SAED pattern of $SrIrO_3$ sample.

To understand the activation process on $SrIrO_3$ perovskite during HER, a simple Ir-based oxide, IrO_2, was also measured for HER under the same operating conditions. In striking contrast, IrO_2 displayed no obvious activation-induced performance enhancement (Figure 2a and b). Meanwhile, the activity of AC-IrO_2 towards HER was quite inferior to that of AC-$SrIrO_3$ (Figure 2a and b). At η = 200 mV, a current density of 30 mA cm^{-2}_{geo} was attained for the AC-$SrIrO_3$ catalyst, which was over one order of magnitude larger than that for the fresh $SrIrO_3$ sample, whereas those for the fresh IrO_2 and AC-IrO_2 were almost equally low, about 1 mA cm^{-2}_{geo} (Figure 2a and b). These results imply that such unique activation-induced performance enhancement in $SrIrO_3$ is probably associated with the perovskite structure, which would be further investigated as below. As a baseline, the HER polarization curve of the benchmark Pt/C catalyst is also given in Figure 2c. A low overpotential of about 116 mV was needed to launch 10 mA cm^{-2}_{geo}, which was only 23 mV smaller than the 139 mV of the AC-$SrIrO_3$ electrode (Figure 2c). By reducing the particle size of the $SrIrO_3$ perovskite through ball milling, the HER apparent activity after activation could be slightly enhanced (named as AC-$SrIrO_3$-BM), with a Pt-like η_{10} of 121 mV (Figure 2c). Tafel plots can reflect the HER kinetics behaviour, and a lower Tafel slope is more

favourable. In our case, AC-$SrIrO_3$, AC-$SrIrO_3$-BM and Pt/C showed the same kinetic mechanism due to having similar Tafel slopes (45-49 mV dec^{-1}), and their smaller slopes suggest faster reaction kinetics than that of AC-IrO_2 (104 mV dec^{-1}) (Figure 2d). More significantly, a more remarkable HER activity for the AC-$SrIrO_3$ electrocatalyst was also observed in a concentrated alkaline medium (1 M KOH), with the overpotential of 72 mV at a 10 mA cm^{-2}_{geo} current density (Figure S3). In addition, compared to the commercialized RuO_2, the AC-$SrIrO_3$ electrocatalyst also showed obviously better HER apparent activity (Figure S3). As a whole, above these data, i.e., η_{10}, and the Tafel slope, demonstrated the outstanding catalytic activity of AC-$SrIrO_3$ among nearly all the reported perovskite oxides for HER in the alkaline electrolyte (Table S3), which also even exceeded numerous other types of representative materials (Table S4)

As is well known, the overall catalytic behaviour of a catalyst generally depends on two critical factors, i.e., the number of active sites and the intrinsic activity of each site. [43, 44] The specific activity (SA), by being normalized to the electrochemical surface area (ECSA), can efficiently reflect the intrinsic activity. The ECSA data of all the oxides can be estimated by CV-based electrochemical double-layer capacitance testing (EDLC, C_{dl}), as can be seen from Figure S4. According to a previous study, the ECSA of the Pt/C catalyst was calculated on the basis of Coulombic charge Q for hydrogen desorption, which is 71 m^2 g^{-1} in 0.1 M KOH. [45] Shown in Figure S5a, and 2e compared the SAs of all the measured samples in 0.1 M KOH. Although AC-$SrIrO_3$ indeed exhibited obviously lower intrinsic activity than the commercial Pt/C catalyst, the SA of AC-$SrIrO_3$ still extensively outperformed those of initial $SrIrO_3$, IrO_2 and AC-IrO_2. Besides, the SA of AC-$SrIrO_3$-BM was nearly coincident with that of AC-$SrIrO_3$, which confirmed the similar intrinsic activity of each active site between them. The relatively small difference between the SAs of IrO_2 and AC-IrO_2 also verified the similar intrinsic activities. Specifically, AC-$SrIrO_3$ had an SA of 0.054 mA cm^{-2}_{ECSA} at η = 200 mV in 0.1 M KOH, which was about 4, 12, and 11 times higher than the 0.014, 0.0045, and 0.005 mA cm^{-2}_{ECSA} of $SrIrO_3$, IrO_2 and AC-IrO_2, respectively. In this study, the HER activity was further revealed by the mass activity (MA) based on the noble metal amount. Evidently, the activated $SrIrO_3$ was much higher than those of other Ir-based contrast samples in 0.1 M KOH(Figure S5b, and 2e). For example, at η = 200 mV, the MA of AC-$SrIrO_3$ was 220 A g^{-1}_{Ir}, lower than that of AC-$SrIrO_3$-BM, but ~11-fold, 42-fold, and 43-fold larger than those of $SrIrO_3$, IrO_2 and AC-IrO_2 (20.2, 5.3, and 5.1 A g^{-1}_{Ir}, respectively). Moreover, when tested in 1 M KOH (Figure S6), the SA and MA of AC-$SrIrO_3$ at η = 200 mV were 0.067 mA cm^{-2}_{ECSA} and 479 A g^{-1}_{Ir}, respectively. These results were evidently comparable to those of some well-known HER catalytic materials (Table S3 and S4). Apart from the prominent HER activity, the AC-$SrIrO_3$ electrode also showed favourable operating durability, as indicated by the almost overlapping LSV curves before and after 5000 CV cycles of testing (Figure S7), and a stable current density of 10 mA cm^{-2}_{geo} over a period of 180 h without any appreciable potential change (Figure 2f).
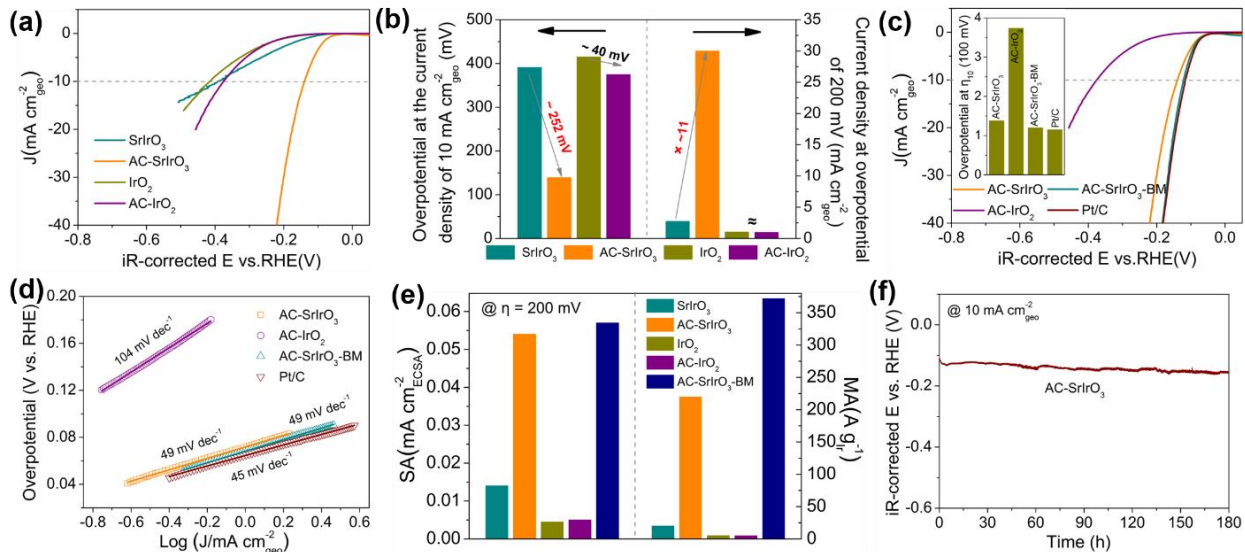
Figure 2. (a) Polarization curves toward HER, and (b) the corresponding activity comparison of overpotential at a current density of 10 mA cm$^{-2}_{geo}$ (left) and current density at an overpotential of 200 mV (right) of SrIrO$_3$, AC-SrIrO$_3$, IrO$_2$ and AC-IrO$_2$ samples in Ar-saturated 0.1 M KOH electrolytes. (c) HER polarization curves of these four catalysts including AC-SrIrO$_3$, AC-SrIrO$_3$-BM, AC-IrO$_2$ and Pt/C. Insert shows overpotential at the 10 mA cm$^{-2}_{geo}$ current density. (d) Tafel plots of AC-SrIrO$_3$, AC-SrIrO$_3$-BM, AC-IrO$_2$ and Pt/C samples, which were derived from (c). (e) Specific activity (SA) and mass activity (MA) of SrIrO$_3$, AC-SrIrO$_3$, IrO$_2$, AC-IrO$_2$, and AC-SrIrO$_3$-BM, respectively, at the overpotential of 200 mV. (f) The stability plot of potential as a function of time at a constant current density of 10 mA cm$^{-2}_{geo}$ for AC-SrIrO$_3$.

To seek the origins of the above-mentioned unique activation-enhanced behaviour during the electrocatalytic HER process and obtain a thorough understanding, these four samples of AC-SrIrO$_3$, SrIrO$_3$, AC-IrO$_2$, and IrO$_2$ were carefully characterized. First, ex-situ X-ray photoelectron spectroscopy (XPS) measurements were carried out to resolve the structural evolution. According to previously reported work, the typical Ir 4f XPS spectra of IrO$_2$ and AC-IrO$_2$ in Figure 3b could be fitted with two doublets and a single satellite peak. [40, 46] The binding energies for the first doublet were 61.88/64.87 eV and 61.79/64.78 eV for IrO$_2$ and AC-IrO$_2$, respectively, which could come from Ir^{4+} in the IrO$_2$ phase, corresponded well to the reported value range. [37, 40, 46] The other doublet with a positive energy shift of ~1.1 eV likely originated from the shake-up satellites of the first doublet for the two samples. In addition, the single satellite peak at a high binding energy of ~67.95 eV was associated with localized non-bonding states. [40, 46] From the above fitting results of Ir 4f XPS spectra from IrO$_2$ and AC-IrO$_2$, there are unnoticeable changes after electrochemical cycling, suggesting that IrO$_2$ possessed a highly stable surface structure in the HER process. Shown in Figure 3a is the deconvoluted Ir 4f XPS spectra of pristine SrIrO$_3$ and AC-SrIrO$_3$. For the pristine SrIrO$_3$ sample, only two doublets were obtained. The first one located at the lower binding energies of 61.86 and 64.84 eV was likely related to Ir^{4+} from a SrIrO$_3$ phase, which was very close to reported data and also located within the reported IrO$_2$ range. [37, 46-48] Similar to that in IrO$_2$, the second one indicated shake-up satellites. Additionally, two analogous doublets within the expected range were also observed in AC-SrIrO$_3$ and their slight difference relative to pristine SrIrO$_3$ hinted a very minor change in the local structural environment of Ir^{4+}. However, noticeably, after electrochemical activation, a pair of additional and intense Ir 4f peaks at 60.95 and 63.93 eV came out in the Ir 4f XPS spectra of AC-SrIrO$_3$ (Figure 3a), which then can be attributed to the signal of metallic Ir (60-61 eV), [49-52] disclosing the surface structural reconstruction. Such significant differences in SrIrO$_3$ and IrO$_2$ during the electrocatalytic process demonstrate the crucial role of surface structural reconstruction in the electrocatalytic activity and reveal that the resulting Ir metal is likely responsible for the enhanced activity of AC-SrIrO$_3$. Moreover, Figure 3c exhibits HR-TEM images of the AC-SrIrO$_3$ sample. After electrochemical activation, apparent structural reconstruction was attained on the surface of AC-SrIrO$_3$ with a depth of around 5 nm, in accordance with the XPS results. When comparing the FFT images from the surface and bulk, such a reconstruction-derived surface was found to be amorphous without long-range ordering. Despite the generation of an amorphous phase, the bulk crystal structure of AC-SrIrO$_3$ was not affected relative to that of fresh monoclinic SrIrO$_3$, as evidenced by the XRD patterns in Figure S8. The Ir oxidation state of the bulk structure was also checked by X-ray absorption spectroscopy (XAS) at the Ir-L$_3$ edge in the fluorescence yield (FY) mode, which is sensitive to the valence of 5d transition metal elements. [53, 54] As shown in Figure 3d, relative to the SrIrO$_3$ spectrum, the lack of energy shift in the AC-SrIrO$_3$ spectrum reflects the negligible valence state change after HER activation in the bulk phase, corresponding to the observation from XRD. EDX results in Figure S9 show that a Sr/Ir molar ratio of ~1 was observed in the inner crystal, while the amorphous surface was mainly composed of Ir, which revealed the element composition well. Upon combining all this obtained characterization evidence, the reconstructed SrIrO$_3$ structure could be identified well. Subsequently, the changes in the ECSA and electrochemical impedance spectroscopy (EIS) for the AC-

SrIrO$_3$ and SrIrO$_3$ electrodes were also evaluated, and the corresponding results are presented in Figure S4, 3e and f. The obtained ECSA of AC-SrIrO$_3$ was nearly 3-fold higher than that of fresh SrIrO$_3$ (Figure 3e). This result disclosed that after electrochemical activation, the SrIrO$_3$ electrode could create more electrocatalytically active sites. By the recorded Nyquist plots in Figure 3f, the AC-SrIrO$_3$ electrode displayed a lower charge transfer resistance (R_{ct}) than the fresh SrIrO$_3$ electrode, implying a faster electron transfer rate for the AC-SrIrO$_3$ electrode. These observations based on ECSA and EIS strongly corresponded to the improved activity and were likely related to the evolution from the microstructure of the electrocatalysts during HER.

Given that the unique surface structure reconstruction solely occurred in monoclinic SrIrO$_3$ and not IrO$_2$, it can be intuitively speculated that surface lattice Sr^{2+} was probably etched during electrochemical cycling and thus induced surface self-reconstruction. According to the XPS results of Sr 3d (Figure 3g), fresh SrIrO$_3$ showed an intense Sr 3d XPS signal while after CV activation, this Sr 3d peak was almost invisible in AC-SrIrO$_3$, which confirmed the appearance of severe Sr leaching during electrochemical cycling. From Figure 3h, the initial molar ratio of Sr and Ir in fresh SrIrO$_3$ was nearly 1, which corresponds to the successful preparation of SrIrO$_3$. After electrochemical activation, about 86% Sr was leached from the SrIrO$_3$ surface. To further verify the etching phenomenon, we monitored the Sr^{2+} ions in the as-used electrolytes by inductively coupled plasma-optical emission spectrometry (ICP). Clearly, a large number of Sr^{2+} ions were detected, as summarized in Figure 3h. Previous works have verified that metal defects can promote surface self-reconstruction during the electrocatalytic process. [25] Accordingly, the leaching of lattice Sr species here might also act as a handle to trigger the reconstruction. More significantly, on the basis of the formation energies for monoclinic SrIrO$_3$ and IrO$_2$ calculated in pioneering studies, the formation energy of monoclinic SrIrO$_3$ being larger than that of IrO$_2$ demonstrated the more unstable nature of monoclinic SrIrO$_3$ (Figure 3i). [55, 56] Thus, surface reconstruction was preferred to happen in monoclinic SrIrO$_3$ during electrochemical activation.
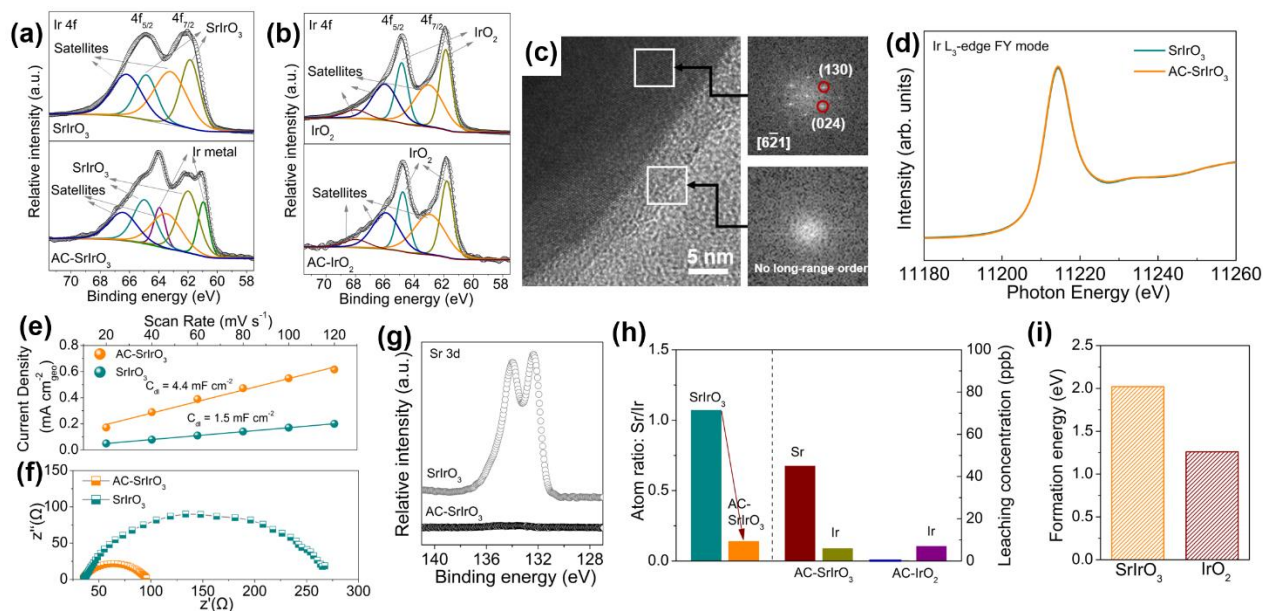
Figure 3. (a, b) High resolution Ir 4f XPS spectra for SrIrO$_3$ ((a) top), AC-SrIrO$_3$ ((b) bottom), IrO$_2$ ((b) top) and AC-IrO$_2$ ((a) bottom) samples. (c) HRTEM image and corresponding fast Fourier transformed (FFT) pattern of AC-SrIrO$_3$. (d) Ir-L$_3$ XAS spectra of SrIrO$_3$ and AC-SrIrO$_3$ in the FY mode. (e) Linear fitting curve (capacitive currents vs. CV scan rates), and (f) EIS Nyquist plots obtained at a potential of -1.1 V vs. Ag|AgCl (3.5 M KCl) for SrIrO$_3$ and AC-SrIrO$_3$. (g) High resolution Sr 3d XPS spectra for SrIrO$_3$ and AC-SrIrO$_3$. (h) The surface atom ratio of Sr and Ir in SrIrO$_3$ and AC-SrIrO$_3$ (left), and leaching concentration of Sr and Ir in SrIrO$_3$ and IrO$_2$ after electrochemical activation (right). (i) Formation energy of SrIrO$_3$ and IrO$_2$.

In addition to the above-mentioned HER catalytic behaviour in 0.1 M KOH, we have also investigated the OER performance of monoclinic SrIrO$_3$ under similar conditions. Interestingly, no obvious activation process was observed during the OER process. The OER polarization curves shown in Figure 4a manifest the outstanding OER activity of SrIrO$_3$ as well. Notably, an extremely low onset potential of 1.43 V at 0.5 mA cm$^{-2}_{geo}$ was observed for the monoclinic SrIrO$_3$ catalyst to effectively drive the OER, while the benchmarked IrO$_2$ offered a relatively higher onset potential of 1.46 V, as reported elsewhere. [57] The overpotential needed to create a current density of 10 mA cm$^{-2}_{geo}$ was only 300 mV for the bulk-phase monoclinic SrIrO$_3$ electrode, which was significantly lower than that of the benchmarked IrO$_2$ (430 mV) and those of most of the perovskite oxides reported in literatures (340-450 mV) (Figure S10). Besides, a smaller Tafel slope (42 mV dec^{-1}) for monoclinic SrIrO$_3$ relative to IrO$_2$ (55 mV dec^{-1}) was also attained, indicating faster OER kinetics (Figure 4b). Moreover, monoclinic SrIrO$_3$ demonstrated the about 2-fold and 5-fold larger SA and MA than IrO$_2$ at η = 320 mV, respectively (Figure S11). Thus, SrIrO$_3$ is clearly also a superior OER electrocatalyst in an alkaline solution, whose activity is comparable to or even better than various typical active OER catalysts reported so

far (Table S5). It is worth noting that a pseudo-cubic SrIrO$_3$(100) film grown on a DyScO$_3$(110) substrate has previously been reported to be a superb OER electrocatalyst in 0.1 M KOH by Suntivich et al. but offered a larger overpotential (η = ~400 mV at 1 mA cm$^{-2}_{geo}$) than our SrIrO$_3$ material and an analogous Tafel slope (40 mV dec^{-1}).[38] By applying the activated monoclinic SrIrO$_3$ electrode via the HER process as an OER electrocatalyst in 0.1 M KOH, a further improved catalytic activity was demonstrated, resulting in a further decrease in the overpotential of around 15 mV to reach a current density of 10 mA cm$^{-2}_{geo}$, i.e., only ~ 285 mV (Figure S12). Such finding suggests that the roles of both electrodes can be easily swapped, thus greatly simplifying the reactor configuration and effectively reducing the fabrication and operation cost for overall water splitting. Shown in Figure S13 is a schematic diagram of a two-electrode water electrolyzer with the same catalyst at both electrodes, which outlines the advantages of such a design.

Accordingly, based on the excellent bifunctionality of monoclinic SrIrO$_3$ regarding the OER and HER, an in-house constructed two-electrode water electrolyzer with monoclinic SrIrO$_3$ bulk materials loaded on a carbon cloth substrate (SrIrO$_3$/CC) as both the anode and the cathode (Figure S13) was built, and its performance for overall water splitting in alkaline solution was tested. It worth noting that SrIrO$_3$/CC as the cathode was first activated through electrochemical cycling to form AC-SrIrO$_3$/CC. As presented in Figure 4c, the coupled AC-SrIrO$_3$/CC//SrIrO$_3$/CC electrodes showed remarkable water-splitting activity, affording a potential of ~1.59 V to get a 10 mA cm$^{-2}_{geo}$ current density (E$_{10}$), which can rival that of the benchmark combination (Pt/C-IrO$_2$) (~1.59 V). With an increase in the applied potential, a rapid current rise was efficiently driven for the AC-SrIrO$_3$/CC//SrIrO$_3$/CC couple, and thereby, this couple clearly outperformed the Pt/C-IrO$_2$ couple in catalyzing water electrolysis when the potential was higher than 1.67 V. We should note that such performance surpassed most of the reported well-known electrocatalysts for overall water splitting (Table S6). In particular, a decent activity for SrIrO$_3$ was realized among perovskite-based materials with excellent bi-functionality, such as electrospun SrNb$_{0.1}$Co$_{0.7}$Fe$_{0.2}$O$_{3-\delta}$ nanorods (E$_{10}$ = ~1.68 V), electrospun La$_{0.5}$(Ba$_{0.4}$Sr$_{0.4}$Ca$_{0.2}$)$_{0.5}$Co$_{0.8}$Fe$_{0.2}$O$_{3-\delta}$ nanorods hybridized with reduced graphene oxide nanosheets (E$_{10}$ = ~1.67 V), and the NdBaMn$_2$O$_{5.5}$ double perovskite (E$_{10}$ = ~1.65 V).[25, 26, 58] Besides, the SrIrO$_3$/CC//AC-SrIrO$_3$/CC cell also maintained robust stability with a negligible change in potential after 10 h of continuous operation at 10 mA cm$^{-2}_{geo}$ (Figure 4d).

A previous representative report has demonstrated that a SrIrO$_3$ thin film with a pseudo-cubic structure prepared under extreme conditions, displays an obvious OER enhancement with time on operation in acidic solution and is a superior OER electrocatalyst that undergoes surface reconstruction with the formation of a SrIrO$_3$/IrO$_x$ composite due to the selective dissolution of SrO.[37] By employing the as-prepared bulk-phase SrIrO$_3$ in the monoclinic structure as a catalyst in an acidic solution, we did observe a slight increase in the performance for OER with time on operation; however, with a further increase in operation time, a deterioration in performance was observed (Figure S14). This phenomenon indicates that a different surface change occurred on bulk SrIrO$_3$ with a monoclinic structure, which was actually not stable for OER catalysis and led to further electrode corrosion (Inset of Figure S14). However, the insightful origins of such differences between these two SrIrO$_3$ materials as acidic OER catalysts have not been revealed and thus require follow-up deep investigation with advanced characterization techniques in the future. On the other hand, as shown in Figure S15, the electrode showed relatively poor activity for HER in acidic solution. These observations then suggest that the pH value of the electrolyte, and the particulate morphology and structure of the electrode material are highly critical for achieving good bi-functionality of a powder-form SrIrO$_3$ electrode for overall water splitting.

As mentioned, in acidic solution, monoclinic SrIrO$_3$ with the conventional powder electrode configuration experienced surface changes during OER, which resulted in slightly improved performance at the initial stage and subsequently degenerated activity. Based on this, we tried to first induce this surface reconstruction process of monoclinic SrIrO$_3$ through OER in acidic acid, and then the reconstructed SrIrO$_3$ was used as a HER electrocatalyst in an alkaline solution. As depicted in Figure S16, after the surface reconstruction under OER conditions in acidic conditions, the electrode showed almost no any catalytic activity for HER in alkaline solution. Such result revealed that the surface reconstruction process was highly dependent on the experimental conditions, while a beneficial effect for electrocatalysis in alkaline solution was achieved only when the electrode was activated under the same conditions.
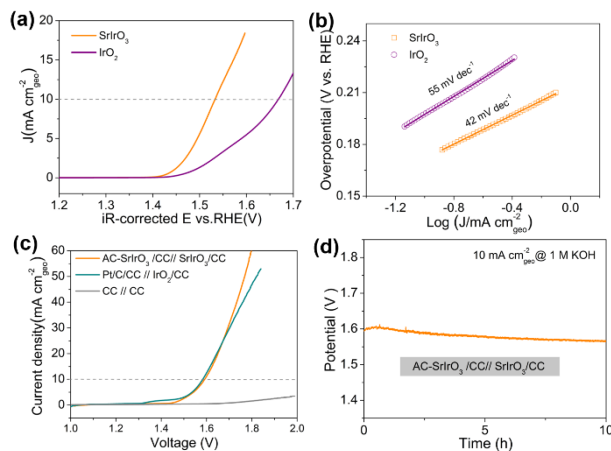
Figure 4. (a) OER polarization curves and (b) the corresponding Tafel plots of SrIrO$_3$ and IrO$_2$ samples in the O$_2$-saturated 0.1 M KOH electrolytes. (c) Water-splitting polarization curves of these three couples including AC-SrIrO$_3$/CC// SrIrO$_3$/CC, Pt/C/CC//IrO$_2$/CC, and blank CC/CC in a 1 M KOH aqueous solution. Catalyst electrode loading: 5 mg cm^{-2}. (d) A chronopotentiometric curve (potential vs. time) of the AC-SrIrO$_3$/CC// SrIrO$_3$/CC system at a fixed current density of 10 mA cm$^{-2}_{geo}$.

3. SUMMARY

In conclusion, a bulk-phase metallic $SrIrO_3$ perovskite with a monoclinic structure was facilely developed with a simple solid-state route without any harsh synthesis conditions. When carrying out a hydrogen-evolution activation process in alkaline solution, monoclinic $SrIrO_3$ delivered continuous reconstruction-enhanced activities owing to lattice Sr^{2+} leaching. Highly outstanding activity and robust stability were finally achieved in the surface reconstruction-derived catalyst AC-$SrIrO_3$, i.e., η_{10} of 139 mV, Tafel slope of 49 mV dec^{-1}, and 180-h stable testing. AC-$SrIrO_3$ also presented the activity at an overpotential of 200 mV that was more than one order of magnitude larger than that in the initial $SrIrO_3$ sample. As substantiated by XPS, XAS, TEM, XRD, and electrochemical analysis, we unambiguously recognized the precise structure of the reconstruction-derived species and demonstrated that the derived active component, strengthened electrical conductivity, and increased active surface areas were responsible for the resulting excellent HER performance. Previous formation-energy calculation results further uncovered that the more unstable nature of $SrIrO_3$ may lead to more favourable self-reconstruction due to the higher formation energy of $SrIrO_3$ in comparison with that of IrO_2. Furthermore, $SrIrO_3$ also showed unprecedented catalytic behaviour for OER in 0.1 M KOH, requiring an overpotential of only 300 mV to reach a current density of 10 mA cm$^{-2}_{geo}$, which was significantly lower than those of most of the perovskite oxides reported in the literature (340-450 mV). And a further enhanced activity by an additional reduction of overpotential of approximately 15 mV at a current density of 10 mA cm$^{-2}_{geo}$ was demonstrated for the activated $SrIrO_3$ electrode from alkaline HER operation. Based on the excellent bifunctionality towards OER and HER of $SrIrO_3$ in a base, an efficient and stable alkaline water electrolyzer with AC-$SrIrO_3$ and $SrIrO_3$ as cathodic and anodic catalysts, respectively, was rationally established, exhibiting a low water-splitting potential of ~1.59 V at a current density of 10 mA cm$^{-2}_{geo}$. Our work not only highlights the significance of surface reconstruction, but also opens a new avenue for further study on perovskite oxides for overall water splitting.

ASSOCIATED CONTENT

Supporting Information.
Catalysts preparation, materials characterizations, electrode preparation and electrochemical measurements, Rietveld refinement results of XRD pattern, some XRD patterns, SEM images, nitrogen adsorption-desorption isotherm curves, LSV and CV curves, surface area, and comparison of HER activity, OER activity, and overall-water-splitting performance for various electrocatalysts. This material is available free of charge via the Internet at http://pubs.acs.org.

AUTHOR INFORMATION

Corresponding Author
*E-mail: zhouwei1982@njtech.edu.cn.
*E-mail: shaozp@njtech.edu.cn
Notes
The authors declare no competing financial interest.

ACKNOWLEDGMENT

REFERENCES

(1) Cao, L. L.; Luo, Q. Q.; Liu, W.; Lin, Y. K.; Liu, X. K.; Cao, Y. J.; Zhang, W.; Wu, Y.; Yang, J. L.; Yao, T.; Wei, S. Q. Identification of Single-atom Active Sites in Carbon-based Cobalt Catalysts During Electrocatalytic Hydrogen Evolution. *Nature Catal.* **2019**, *2*, 134-141.

(2) Vojvodic, A.; Norskov, J. K. Optimizing Perovskites for the Water-Splitting Reaction. *Science* **2011**, *334*, 1355-1356.

(3) Yu, J.; Guo, Y.; She, S.; Miao, S.; Ni, M.; Zhou, W.; Liu, M.; Shao, Z. Bigger is Surprisingly Better: Agglomerates of Larger RuP Nanoparticles Outperform Benchmark Pt Nanocatalysts for the Hydrogen Evolution Reaction. *Adv. Mater.* **2018**, *30*, 1800047.

(4) Zheng, Y.; Jiao, Y.; Zhu, Y.; Li, L. H.; Han, Y.; Chen, Y.; Jaroniec, M.; Qiao, S.-Z. High Electrocatalytic Hydrogen Evolution Activity of an Anomalous Ruthenium Catalyst. *J. Am. Chem. Soc.* **2016**, *138*, 16174-16181.

(5) Liu, B.; Zhao, Y. F.; Peng, H. Q.; Zhang, Z. Y.; Sit, C. K.; Yuen, M. F.; Zhang, T. R.; Lee, C. S.; Zhang, W. J. Nickel-Cobalt Diselenide 3D Mesoporous Nanosheet Networks Supported on Ni Foam: An All-pH Highly Efficient Integrated Electrocatalyst for Hydrogen Evolution. *Adv. Mater.* **2017**, *29*, 1606521.

(6) You, B.; Jiang, N.; Sheng, M.; Gul, S.; Yano, J.; Sun, Y. J. High-Performance Overall Water Splitting Electrocatalysts Derived from Cobalt-Based Metal-Organic Frameworks. *Chem. Mater.* **2015**, *27*, 7636–7642.

(7) Yu, J.; Zhong, Y.; Wu, X.; Sunarso, J.; Ni, M.; Zhou, W.; Shao, Z. Bifunctionality from Synergy: CoP Nanoparticles Embedded in Amorphous CoOx Nanoplates with Heterostructures for Highly Efficient Water Electrolysis. *Adv. Sci.* **2018**, *5*, 1800514.

(8) Menezes, P. W.; Indra, A.; Zaharieva, I.; Walter, C.; Loos, S.; Hoffmann, S.; Schlogl, R.; Dau, H.; Driess, M. Helical Cobalt Borophosphates to Master Durable Overall Water-Splitting. *Energy Environ. Sci.* **2019**, *12*, 988-999.

(9) Lyu, F.; Wang, Q.; Choi, S. M.; Yin, Y. Noble-Metal-Free Electrocatalysts for Oxygen Evolution. *Small* **2019**, *15*, 1804201.

(10) Yu, P.; Wang, F.; Shifa, T. A.; Zhan, X.; Lou, X.; Xia, F.; He, J. Earth Abundant Materials Beyond Transition Metal Dichalcogenides: A Focus on Electrocatalyzing Hydrogen Evolution Reaction. Nano *Energy* **2019**, *58*, 244-276.

(11) Yu, J.; He, Q.; Yang, G.; Zhou, W.; Shao, Z.; Ni, M. Recent Advances and Prospective in Ruthenium-Based Materials for Electrochemical Water Splitting. *ACS Catal.* **2019**, *9*, 9973-10011.

(12) Lei, C.; Wang, Y.; Hou, Y.; Liu, P.; Yang, J.; Zhang, T.; Zhuang, X.; Chen, M.; Yang, B.; Lei, L. Efficient Alkaline Hydrogen Evolution on Atomically Dispersed Ni-Nx Species Anchored Porous Carbon with Embedded Ni Nanoparticles by Accelerating Water Dissociation Kinetics. *Energy Environ. Sci.* **2019**, *12*, 149-156.

(13) Das, D.; Nanda, K. K. One-Step, Integrated Fabrication of Co$_2$P Nanoparticles Encapsulated N, P Dual-Doped CNTs for Highly Advanced Total Water Splitting. *Nano Energy* **2016**, *30*, 303-311.

(14) Hwang, J.; Rao, R. R.; Giordano, L.; Katayama, Y.; Yu, Y.; Shao-Horn, Y. Perovskites in Catalysis and Electrocatalysis. *Science* **2017**, *358*, 751-756.

(15) Zhu, Y.; Zhou, W.; Yu, J.; Chen, Y.; Liu, M.; Shao, Z. Enhancing Electrocatalytic Activity of Perovskite Oxides by Tuning Cation Deficiency for Oxygen Reduction and Evolution Reactions. *Chem. Mater.* **2016**, *28*, 1691-1697.

(16) Zhu, Y.; Zhou, W.; Sunarso, J.; Zhong, Y.; Shao, Z. Phosphorus-Doped Perovskite Oxide as Highly Efficient Water Oxidation Electrocatalyst in Alkaline Solution. *Adv. Funct. Mater.* **2016**, *26*, 5862-5872.

(17) Zhu, Y.; Dai, J.; Zhou, W.; Zhong, Y.; Wang, H.; Shao, Z. Synergistically Enhanced Hydrogen Evolution Electrocatalysis by in Situ Exsolution of Metallic Nanoparticles on Perovskites. *J. Mater. Chem. A* **2018**, *6*, 13582-13587.

(18) Xu, X.; Wang, W.; Zhou, W.; Shao, Z. Recent Advances in Novel Nanostructuring Methods of Perovskite Electrocatalysts for Energy-Related Applications. *Small Methods* **2018**, *2*, 1800071.

(19) Zhang, H.; Guan, D.; Gao, X.; Yu, J.; Chen, G.; Zhou, W.; Shao, Z. Morphology, Crystal Structure and Electronic State One-Step Co-tuning Strategy Towards Developing Superior Perovskite Electrocatalysts for Water Oxidation. *J. Mater. Chem. A* **2019**, *7*, 19228-19233.

(20) Xiong, J.; Zhong, H.; Li, J.; Zhang, X.; Shi, J.; Cai, W.; Qu, K.; Zhu, C.; Yang, Z.; Beckman, S. P.; Cheng, H. Engineering Highly Active Oxygen Sites in Perovskite Oxides for Stable and Efficient Oxygen Evolution. *Appl. Catal. B-Environ.* **2019**, *256*, 117817.

(21) Ling, T.; Yan, D.-Y.; Wang, H.; Jiao, Y.; Hu, Z.; Zheng, Y.; Zheng, L.; Mao, J.; Liu, H.; Du, X.-W., Activating Cobalt (II) Oxide Nanorods for Efficient Electrocatalysis by Strain Engineering. *Nat. Commun.* **2017**, *8*, 1509

(22) Zheng, T.; Sang, W.; He, Z.; Wei, Q.; Chen, B.; Li, H.; Cao, C.; Huang, R.; Yan, X.; Pan, B., Conductive Tungsten Oxide Nanosheets for Highly Efficient Hydrogen Evolution. *Nano Lett.* **2017**, *17*, 7968 -7973.

(23) Xu, X.; Chen, Y.; Zhou, W.; Zhu, Z.; Su, C.; Liu, M.; Shao, Z. A Perovskite Electrocatalyst for Efficient Hydrogen Evolution Reaction. *Adv. Mater.* **2016**, *28*, 6442-6448

(24) Zhang, Z.; Chen, Y.; Dai, Z.; Tan, S. Z.; Chen, D. Promoting Hydrogen-Evolution Activity and Stability of Perovskite Oxides via Effectively Lattice Doping of Molybdenum. *Electrochim. Acta* **2019**, *312*, 128-136.

(25) Zhu, Y.; Zhou, W.; Zhong, Y.; Bu, Y.; Chen, X.; Zhong, Q.; Liu, M.; Shao, Z. A Perovskite Nanorod as Bifunctional Electrocatalyst for Overall Water Splitting. *Adv. Energy Mater.* **2017**, *7*, 1602122.

(26) Hua, B.; Li, M.; Zhang, Y. Q.; Sun, Y. F.; Luo, J. L. All-In-One Perovskite Catalyst: Smart Controls of Architecture and Composition toward Enhanced Oxygen/Hydrogen Evolution Reactions. *Adv. Energy Mater.* **2017**, *7*, 1700666.

(27) Wang, J.; Xu, F.; Jin, H.; Chen, Y.; Wang, Y. Non-Noble Metal-based Carbon Composites in Hydrogen Evolution Reaction: Fundamentals to Applications. *Adv. Mater.* **2017**, *29*, 1605838.

(28) Guan, D.; Zhou, J.; Hu, Z.; Zhou, W.; Xu, X.; Zhong, Y.; Liu, B.; Chen, Y.; Xu, M.; Lin, H. -J.; Chen, C. -T.; Wang, J. -Q.; Shao, Z. Searching General Sufficient-and-Necessary Conditions for Ultrafast Hydrogen-Evolving Electrocatalysis. *Adv. Funct. Mater.* **2019**, *29*, 1900704.

(29) Guan, D.; Zhou, J.; Huang, Y. -C.; Dong, C. -L.; Wang, J. -Q.; Zhou, W.; Shao, Z. Screening Highly Active Perovskites for Hydrogen-Evolving Reaction via Unifying Ionic Electronegativity Descriptor. *Nat. Commun.* **2019**, *10*, 3755.

(30) He, Q.; Wan, Y.; Jiang, H.; Pan, Z.; Wu, C.; Wang, M.; Wu, X.; Ye, B.; Ajayan, P. M.; Song, L. Nickel Vacancies Boost Reconstruction in Nickel Hydroxide Electrocatalyst. *ACS Energy Lett.* **2018**, *3*, 1373-1380.

(31) Jiang, H.; He, Q.; Li, X.; Su, X.; Zhang, Y.; Chen, S.; Zhang, S.; Zhang, G.; Jiang, J.; Luo, Y. Tracking Structural Self-Reconstruction and Identifying True Active Sites toward Cobalt Oxychloride Precatalyst of Oxygen Evolution Reaction. *Adv. Mater.* **2019**, *31*, 1805127

(32) Zhang, B.; Jiang, K.; Wang, H.; Hu, S. Fluoride-Induced Dynamic Surface Self-Reconstruction Produces Unexpectedly Efficient Oxygen-Evolution Catalyst. *Nano Lett.* **2018**, *19*, 530-537.

(33) Lv, C.; Xu, S.; Yang, Q.; Huang, Z.; Zhang, C. Promoting Electrocatalytic Activity of Cobalt Cyclotetraphosphate in Full Water Splitting by Titanium-Oxide-Accelerated Surface Reconstruction. *J. Mater. Chem. A* **2019**, *7*, 12457-12467.

(34) Tu, W.; Chen, K.; Zhu, L.; Zai, H.; E, B.; Ke, X.; Chen, C.; Sui, M.; Chen, Q.; Li, Y. Tungsten-Doping-Induced Surface Reconstruction of Porous Ternary Pt-Based Alloy Electrocatalyst for Oxygen Reduction. *Adv. Funct. Mater.* **2019**, *29*, 1807070.

(35) Jiang, H.; He, Q.; Zhang, Y.; Song, L. Structural Self-reconstruction of Catalysts in Electrocatalysis. *Accounts Chem. Res.* **2018**, *51*, 2968-2977.

(36) Jang, S. Y.; Kim, H.; Moon, S. J.; Choi, W. S.; Jeon, B. C.; Yu, J.; Noh, T. W. The Electronic Structure of Epitaxially Stabilized 5d Perovskite $Ca_{1-x}Sr_xIrO_3$ (x= 0, 0.5, and 1) Thin Films: The Role of Strong Spin-Orbit Coupling. *J. Phys.: Condens. Matter* **2010**, *22*, 485602.

(37) Seitz, L. C.; Dickens, C. F.; Nishio, K.; Hikita, Y.; Montoya, J.; Doyle, A.; Kirk, C.; Vojvodic, A.; Hwang, H. Y.; Norskov, J. K. A Highly Active and Stable $IrO_x/SrIrO_3$ Catalyst for the Oxygen Evolution Reaction. *Science* **2016**, *353*, 1011-1014.

(38) Tang, R.; Nie, Y.; Kawasaki, J. K.; Kuo, D. -Y.; Petretto, G.; Hautier, G.; Rignanese, G. -M.; Shen, K. M.; Schlom, D. G.; Suntivich, J. Oxygen Evolution Reaction Electrocatalysis on $SrIrO_3$ Grown Using Molecular Beam Epitaxy. *J. Mater. Chem. A* **2016**, *4*, 6831-6836.

(39) Zhu, Y.; Zhou, W.; Chen, Z. G.; Chen, Y.; Su, C.; Tadé, M. O.; Shao, Z. $SrNb_{0.1}Co_{0.7}Fe_{0.2}O_{3-\delta}$ Perovskite as a Next-generation Electrocatalyst for Oxygen Evolution in Alkaline Solution. *Angew. Chem. Int. Ed.* **2015,** *54*, 3897-3901.

(40) Chen, Y.; Li, H.; Wang, J.; Du, Y.; Xi, S.; Sun, Y.; Sherburne, M.; Ager, J. W.; Fisher, A. C.; Xu, Z. J. Exceptionally Active Iridium Evolved from a Pseudo-Cubic Perovskite for Oxygen Evolution in Acid. *Nat. Commun.* **2019,** *10*, 572.

(41) Wang, S.; Wang, J.; Zhu, M.; Bao, X.; Xiao, B.; Su, D.; Li, H.; Wang, Y. Molybdenum-Carbide-Modified Nitrogen-Doped Carbon Vesicle Encapsulating Nickel Nanoparticles: a Highly Efficient, Low-cost Catalyst for Hydrogen Evolution Reaction. *J. Am. Chem. Soc.* **2015**, *137*, 15753-15759.

(42) Zhu, Y.; Chen, G.; Xu, X.; Yang, G.; Liu, M.; Shao, Z. Enhancing Electrocatalytic Activity for Hydrogen Evolution by Strongly Coupled Molybdenum Nitride@ Nitrogen-doped Carbon Porous Nano-octahedrons. *ACS Catal.* **2017,** *7*, 3540-3547.

(43) Seh, Z. W.; Kibsgaard, J.; Dickens, C. F.; Chorkendorff, I.; Nørskov, J. K.; Jaramillo, T. F. Combining Theory and Experiment in Electrocatalysis: Insights into Materials Design. *Science* **2017**, *355*, eaad4998.

(44) Zhu, Y.; Tahini, H. A.; Hu, Z.; Dai, J.; Chen, Y.; Sun, H.; Zhou, W.; Liu, M.; Smith, S. C.; Wang, H.; Shao, Z. Unusual Synergistic Effect in Layered Ruddlesden-Popper Oxide Enables Ultrafast Hydrogen Evolution. *Nat. Commun.* **2019**, *10*, 149.

(45) Han, X.; Cheng, F.; Zhang, T.; Yang, J.; Hu, Y.; Chen, J. Hydrogenated Uniform Pt Clusters Supported on Porous $CaMnO_3$ as a Bifunctional Electrocatalyst for Enhanced Oxygen Reduction and Evolution. *Adv. Mater.* **2014**, *26*, 2047-2051.

(46) Pfeifer, V.; Jones, T. E.; Velasco Velez, J. J.; Massue, C.; Greiner, M. T.; Arrigo, R.; Teschner, D.; Girgsdies, F.; Scherzer, M.; Allan, J.; Hashagen, M.; Weinberg, G.; Piccinin, S.; Havecker, M.; Knop-Gerickea, A.; Schloglac, R. The Electronic Structure of Iridium Oxide Electrodes Active in Water Splitting. *Phys. Chem. Chem. Phys.* **2016**, *18*, 2292-2296.

(47) Liu, Y.; Masumoto, H.; Goto, T. Structural, Electrical and Optical Characterization of $SrIrO_3$ Thin Films Prepared by Laser-Ablation. *Mater. Trans.* **2005**, *46*, 100-104.

(48) Strickler, A. L.; Higgins, D.; Jaramillo, T. F. Crystalline Strontium Iridate Particle Catalysts for Enhanced Oxygen Evolution in Acid. *ACS Appl. Energy Mater.* **2019**, *2*, 5490-5498.

(49) Marinova, T. S.; Kostov, K. L. Adsorption of Acetylene and Ethylene on A Clean Ir (111) Surface. *Surf. Sci.* **1987**, *181*, 573-585.

(50) Peuckert, M. XPS Investigation of Surface Oxidation Layers on A Platinum Electrode in Alkaline Solution. *Electrochim. Acta* **1984**, *29*, 1315-1320.

(51) Minguzzi, A.; Locatelli, C.; Lugaresi, O.; Achilli, E.; Cappelletti, G.; Scavini, M.; Coduri, M.; Masala, P.; Sacchi, B.; Vertova, A.; Ghigna, P.; Rondinini, S. Easy Accommodation of Different Oxidation States in Iridium Oxide Nanoparticles with Different Hydration Degree as Water Oxidation Electrocatalysts. *ACS Catal.* **2015**, *5*, 5104-5115.

(52) Gong, S.; Wang, C.; Jiang, P.; Yang, K.; Lu, J.; Huang, M.; Chen, S.; Wang J.; Chen Q. O Species-Decorated Graphene Shell Encapsulating Iridium-Nickel Alloy as An Efficient Electrocatalyst towards Hydrogen Evolution Reaction. *J. Mater. Chem. A* **2019**, *7*, 15079-15088.

(53) Paul, A. K.; Sarapulova, A.; Adler, P.; Reehuis, M.; Kanungo, S.; Mikhailova, D.; Schnelle, W.; Hu, Z. W.; Kuo, C. Y.; Siruguri, V.; Rayaprol, S.; Soo , Y. L.; Yan, B. H.; Felser, C.; Tjeng, L. H.; Jansen, M. Magnetically Frustrated Double Perovskites: Synthesis, Structural Properties, and Magnetic Order of Sr_2BOsO_6 (B= Y, In, Sc). *Z. Anorg. Allg. Chem.* **2015**, *641*, 197-205.

(54) Agrestini, S.; Chen, K.; Kuo, C. -Y.; Zhao, L.; Lin, H. -J.; Chen, C. -T.; Rogalev, A.; Ohresser, P.; Chan, T.-S.; Weng, S.-C.; Auffermann, G.; Völzke, A.; Komarek, A. C.; Yamaura, K.; Haverkort, M. W.; Hu, Z.; Tjeng, L. H. Nature of the Magnetism of Iridium in the Double Perovskite Sr_2CoIrO_6. *Phys. Rev. B* **2019**, *100*, 014443.

(55) Materials Project Optimized Structure. http://www.materialsproject.org.

(56) Duan, Y.; Sun, S.; Sun, Y.; Xi, S.; Chi, X.; Zhang, Q.; Ren, X.; Wang, J.; Ong, S. J. H.; Du, Y., Mastering Surface Reconstruction of Metastable Spinel Oxides for Better Water Oxidation. *Adv. Mater.* **2019**, *31*, 1807898.

(57) Zhu, Y.; Zhou, W.; Chen, Y.; Yu, J.; Liu, M.; Shao, Z. A High-Performance Electrocatalyst for Oxygen Evolution Reaction: $LiCo_{0.8}Fe_{0.2}O_2$. *Adv. Mater.* **2015**, *27*, 7150-7155.

(58) Wang, J.; Gao, Y.; Chen, D.; Liu, J.; Zhang, Z.; Shao, Z.; Ciucci, F. Water Splitting with an Enhanced Bifunctional Double Perovskite. *ACS Catal.* **2018**, *8*, 364-371.

SYNOPSIS TOC:

Table of Contents